


Quantum Repeaters with Encoding on Nitrogen-Vacancy-Center Platforms

Yumang Jing^{*} and Mohsen Razavi

School of Electronic and Electrical Engineering, University of Leeds, Leeds LS2 9JT, United Kingdom

 (Received 30 May 2021; revised 13 June 2022; accepted 28 June 2022; published 16 August 2022)

We investigate quantum repeater protocols that rely on three-qubit repetition codes using nitrogen-vacancy (N-V) centers in diamond as quantum memories. N-V centers offer a two-qubit register, corresponding to their electron and nuclear spins, which makes it possible to perform deterministic two-qubit operations within one N-V center. For quantum repeater applications, however, we need to do joint operations on two separate N-V centers. Here, we study two N-V-center-based repeater structures that enable such deterministic joint operations. One structure offers less consumption of classical communication, at the cost of more computation overhead, whereas the other relies on a smaller number of physical resources and operations. We assess and compare their performance for the task of secret-key generation under the influence of noise and decoherence with current and near-term experimental parameters. We quantify the regimes of operation where one structure outperforms the other, and find the regions where encoded quantum repeaters offer practical advantages over their nonencoded counterparts.

DOI: [10.1103/PhysRevApplied.18.024041](https://doi.org/10.1103/PhysRevApplied.18.024041)

I. INTRODUCTION

The unavoidable transmission loss in optical channels poses a serious challenge to distributing entanglement between remote parties. A key solution to this problem is to use quantum repeaters (QRs) [1,2], which are the main building blocks of future quantum communication networks. The conventional idea behind QRs is to create entanglement over shorter segments, followed by entanglement swapping (ES) at all intermediate nodes to distribute entanglement over a long distance [1]. Doing ES operations in a nested way can result in accumulation of errors in the system, for which entanglement-distillation (ED) techniques have been proposed [2]. An attractive option for implementing a repeater chain is based on using probabilistic ES operations [3,4], e.g., by using linear optics, and/or probabilistic ED procedures [5,6]. However, due to the probabilistic nature of such operations, the finite coherence time of the currently available quantum memories (QMs) can restrict the performance of such systems. Nevertheless, as quantum technologies make progress, other promising experimental platforms are emerging in which at least some of the previous probabilistic steps can be performed in a deterministic way. In this paper, we focus on one such possible implementation, where both ES and ED operations are performed in a deterministic way. We particularly investigate the suitability of nitrogen-vacancy (N-V) centers in diamond in such settings.

In order to perform ES and ED operations in a deterministic way, we need not only a suitable physical platform that allows deterministic two-qubit gates, but also a repeater protocol that allows one-way ED. One approach to deterministic ED operations is based on quantum repeaters with encoding [7]. Such repeaters rely on quantum error-correction (QEC) codes for their ED operations, and in doing so they get around the bottleneck caused by the transmission delays in acknowledging the success of ES and ED operations. In this protocol, the entangled states over elementary links are in encoded forms, such that errors in the ES steps can potentially be detected and corrected. That is, the ED operation is effectively performed via a QEC framework. This results in less waiting time, and thus less restriction on the QM coherence times, and can boost the entanglement generation rate in a QR. Such an approach is, however, possible only in QM platforms that allow the deterministic gates needed for ES and QEC operations.

In this paper, we study the use of N-V centers as a platform for QRs with encoding. This is partly driven by the successful implementation of deterministic two-qubit gates between the electron and nuclear spins of a single N-V center [8–10]. Moreover, such memories have been adopted for the demonstration of a simple QR network between four cities in the Netherlands [11,12]. This offers a promising platform for the implementation of encoded QR structures in the near future, as our recent work on QRs with encoding [13,14] suggests that a simple three-qubit repetition code could be the best option in such repeaters for quantum-key-distribution (QKD) applications over

^{*}yumangjing@gmail.com

short to moderately long distances. In particular, we find that there are regimes of operation where encoded QRs can outperform probabilistic QRs [14]. This means that for the type of networks that we are expecting to have in the short term, it could be a rewarding exercise to implement encoded QRs despite their additional implementation challenges.

To get a sensible view of the requirements versus gains for $N-V$ -center-based QRs with encoding, we need to consider realistic scenarios in which such memories can be used. Although in earlier work by our group [13,14] the performance of QRs with three-qubit repetition codes was carefully studied in the presence of operational errors, such analyses are not directly applicable to the case of $N-V$ centers. Firstly, the work presented in Refs. [13,14] assumes that a direct deterministic Bell-state measurement (BSM) on two separate QMs is readily available. This is not exactly the case for $N-V$ centers. While it is possible to use an entangled link between the electron spins of two $N-V$ centers to mediate a joint operation on them [15], we need to account for any additional errors or delays that this may cause. There are also different QR structures that we can then come up with based on this mediatory entangled link, which need to be comparatively studied. Finally, the work presented in Refs. [13,14] ignores the impact of memory decoherence. Now that we have chosen a memory, which is short of ideal once it gets to coherence times, we need to consider its effect on the performance to make a better assessment of the system requirements.

In this paper, motivated by the ideas and structures in Refs. [15,16], we propose two structures for encoded QRs with $N-V$ centers. One structure has the advantage of requiring less consumption of classical communication, while the other uses fewer resources. We assess and compare their performance in generating secret keys under the influence of erroneous operations and decoherence, using current or near-term experimental parameters. We compare the results with those for simpler nonencoded structures where deterministic BSMs are employed but no ED operation is applied. Our results suggest that while at short distances the nonencoded schemes may offer better performance, as we go to longer distances it pays off use structures that employ more encoded links. As the experimental parameters, e.g., memory coherence times, improve, the encoded structure that uses fewer resources often offer the best performance among those considered in this paper. We also specify the gap between what we have experimentally available today versus the minimum specifications required for any of these systems to work.

The paper is structured as follows. In Sec. II, we begin with a description of an ideal implementation of encoded QRs motivated by Refs. [7,17] on $N-V$ -center-based platforms, and explain the error models that we use to formulate the problem at hand. In Sec. III, we analyze the effect of decoherence, as well as other system imperfections, on

system performance, and calculate the secret-key generation rates for such setups in Sec. IV. We compare our results with the case of QRs without encoding and illustrate the parameter regions where one type of protocol outperforms the others. Finally, we conclude the paper in Sec. V.

II. SYSTEM DESCRIPTION

In this paper, we study the implementation of QRs with encoding on $N-V$ -center platforms. One of the key features of $N-V$ centers, which makes them a desirable option for QR setups, is that they are two-qubit registers. This includes an electron spin that can act as an optical interface with single photons, and a nuclear spin, due to carbon or nitrogen atoms neighboring the vacancy, suitable for long-time quantum storage. Moreover, using microwave and radio-frequency signals, two-qubit operations, e.g., controlled-NOT (CNOT) and controlled-phase gates, can be performed deterministically on these two qubits within each $N-V$ center [18,19]. Within each $N-V$ center, one can also map a quantum state from the electron to the nuclear spin and vice versa [20–23]. All these tools come handy for dealing with the operations that we need in the QR setup.

An additional requirement for an efficient QR setup is the ability to write and read single photons to and from a QM. By driving an $N-V$ center embedded in a diamond crystal with a laser field, we can drive many transitions that mostly involve vibrational-mode phonons. Such transitions are not useful for coherent operations, as these vibrational modes often quickly die out within the crystal. Zero-phonon-line (ZPL) emissions are then effectively the key to generating entangled states with $N-V$ centers. Even at near-zero-kelvin temperatures, however, such emissions account for typically only a small portion, around 3%, of all radiation from the $N-V$ center [24]. Considering also the low collection efficiency from a bulk crystal, entanglement generation with $N-V$ centers has been extremely inefficient [25]. A remedy to both of these problems, of ZPL emission rates and collection efficiency, is to have a microcavity around the $N-V$ center [26–29]. There have been several efforts in this regard, which have improved the ZPL emission rates to 46% and have increased the collection efficiency by a factor of several times [30–32]. In this paper, we assume that cavity-based $N-V$ -center platforms are available, and use known techniques with this technology to entangle light with $N-V$ centers and perform quantum operations and measurements on them. These tools are summarized in Sec. II A, based on which we explain several QR protocols and structures, and then finish that section with our error models. Note that the methodologies developed here are also applicable to a broader class of two-qubit memories, including silicon-vacancy centers [33].

Throughout the paper, we denote electron (nuclear) spins by lowercase (uppercase) letters; for instance, if $|0\rangle_a$ and $|1\rangle_a$ represent the basis vectors corresponding to electron spin numbers $m_S = 0$ and $m_S = -1$, respectively, then $|0\rangle_A$ and $|1\rangle_A$ represent the basis vectors corresponding to the nuclear spin numbers $m_I = 0$ and $m_I = -1$, respectively, of the same N- V center.

A. N- V Center as a Toolbox

Here, we explain how specific features of N- V centers can be used to implement the main components of encoded QRs.

1. Entanglement distribution

One of the key ingredients of QR protocols is establishing entangled states over elementary links. Suppose we want to share an entangled state $|\Phi^+\rangle_{AB} = 1/\sqrt{2}(|00\rangle_{AB} + |11\rangle_{AB})$ between nuclear spins A and B . We can first share an entangled state between the corresponding electron spins a and b , and then map the state of a (b) to A (B). This mapping is performed by initializing the nuclear spins in $|00\rangle_{AB}$, performing CNOT gates within each N- V center with the electron spin as the control qubit, and then measuring the electron spins in the X basis.

There are several schemes for distributing entangled states between the electron spins of two remote N- V centers. In most of them, the entanglement distribution involves generating a spin-photon entanglement at each end of the link and then swapping entanglement in the middle of the link [34–36]. Depending on whether the spin-photon entanglement is in one optical mode (i.e., a zero- or one-photon space), or two (e.g., the polarization, or time-bin, space), the BSM in the middle may rely on single-mode or two-mode interference. If the BSM is conclusive, then the entanglement distribution task is heralded to be successful; otherwise, it needs to be repeated until success is achieved. The schemes that rely on single-mode interference often require one photon to travel safely to the middle of the link, and hence may have better rate scaling with distance for heralding success. However, in order to obtain a high-fidelity entangled state, we need to either keep the spin-photon entanglement generation rate very low (e.g., around 1%) [12,37–39] or rerun the procedure to distill the entangled state [29,35,40,41]. In both cases the effective success rate, in certain regimes of interest in the context of the present work, could then become comparable to those of the two-mode schemes, where the rate decays exponentially with the distance between nodes A and B . For instance, in our setup, where the length of the optimum elementary link is typically below 20 km, the extra channel loss in the two-mode case is a small factor, although one also has to account for additional coupling or detector efficiencies. But, aside from the success rate of entanglement generation, another important factor is the

amount of initial noise, or loss in fidelity, that we can tolerate in our system. The two-mode schemes can, in principle, generate ideal entangled states, whereas, in the single-mode schemes, some errors are inevitable, due to, e.g., generating one photon at each end. In a real experiment, one has to factor in all these nuances, as well as practical restrictions on the system, to decide which entanglement distribution scheme may work best in that setting.

In order to encompass the essence of the different entanglement distribution schemes available, we assume here that a generic two-mode entanglement distribution scheme is used where, at each of the nodes A and B , the polarization of a single photon is entangled with the electron spin of the N- V center (see Refs. [42,43], for example). These photons are frequency converted, if needed, and are then coupled to an optical channel. Using linear optics and single-photon detectors, a partial BSM in the polarization basis is then performed on these two photons in the middle of the link. Once a successful BSM is heralded, this information is sent back to nodes A and B , at which point the state of the electron spins is transferred to and stored in the corresponding nuclear spins. We model the generated entangled state as a Werner state, as explained later in Sec. II C. Note that any other entanglement distribution scheme can also be analyzed similarly using the techniques and procedures presented in this paper.

2. Encoded entanglement distribution

In this paper, we consider encoded QRs with three-qubit repetition codes, where the logical qubits are encoded as

$$|\tilde{0}\rangle = |000\rangle \quad \text{and} \quad |\tilde{1}\rangle = |111\rangle, \quad (1)$$

and where $|0\rangle$ and $|1\rangle$ represent the standard basis for a single qubit. This code can correct up to one bit-flip error. Although this is not a strong error-correction code, it has been shown in our previous work that if we rely on its error-detection features it offers reasonable performance at short and moderately long distances [13,14] as compared with more complicated codes. We therefore analyze this particular code for our N- V -center platform.

The first step in an encoded QR is to ideally distribute the encoded entangled states in the following form:

$$|\tilde{\Phi}^+\rangle_{AB} = \frac{1}{\sqrt{2}}(|\tilde{0}\tilde{0}\rangle_{AB} + |\tilde{1}\tilde{1}\rangle_{AB}), \quad (2)$$

where here we consider two example memory banks $\mathbf{A} = (A_1, A_2, A_3)$ and $\mathbf{B} = (B_1, B_2, B_3)$ at the two ends of an elementary link. To this end, using the scheme described in Sec. II A 1, we first generate Bell pairs $|\Phi^+\rangle_{A_i B_i} = 1/\sqrt{2}(|00\rangle_{A_i B_i} + |11\rangle_{A_i B_i})$, for $i = 1, 2, 3$. Once electron spins are available again in all N- V centers of the memory banks \mathbf{a} and \mathbf{b} , we initialize them in the codeword

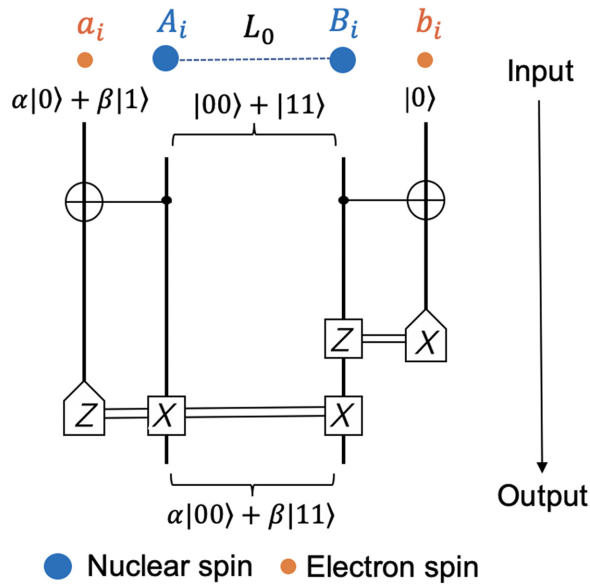


FIG. 1. Quantum circuit for remote CNOT gate. Note that single-qubit measurements (trapezoidal boxes) are performed on electron spins. Here, a_i - A_i represents the electron and nuclear spins in one N- V center separated by a distance L_0 from the corresponding N- V center, b_i - B_i , at the other end of the elementary link.

states $1/\sqrt{2}(|\tilde{0}\rangle_a + |\tilde{1}\rangle_a)$ and $|\tilde{0}\rangle_b$. Finally, using transverse remote CNOT gates, shown in Fig. 1, we can generate the state in Eq. (2) [7]. The same procedure is applied to all elementary links.

Note that the remote CNOT circuit in Fig. 1 is slightly different from the one used in Refs. [13,14]. In the latter work, the remote CNOT circuit requires measurements on qubits that hold the initial Bell state, i.e., the nuclear spins in our N- V -center setup. In N- V centers, however, a nuclear spin is often measured by first mapping its state to an electron spin, using a CNOT gate, and then measuring the electron spin [23,44]. This is not, however, possible in our case, as this would ruin the initial state of the electron spins. We therefore slightly change the remote CNOT circuit such that the measurements are done only on electron spins, with the nuclear spins always in an entangled state.

3. Entanglement swapping

Once encoded entangled states have been distributed between the nuclear spins across all elementary links, the next step is to perform ES operations at all intermediate stations to extend the entanglement to the entire link. In the encoded repeater protocol, this can be done by performing BSMs, in a transverse way, on corresponding pairs of N- V centers at each of the intermediate nodes. This operation also allows us to pick up some of the errors that might have been accumulated by this stage, and helps us

distill the final entangled state. For instance, in the three-qubit repetition code considered here, the BSM is made of an X and a Z operator measurement, the results of which specify the type of encoded Bell state that will be shared between the remote nodes. Ideally, the result of the Z operator measurement must be 000 or 111. Because of errors in the system, however, we may get other combinations of 0 and 1, which correspond to detecting an error. A majority rule can be used here to specify the most likely post-BSM encoded Bell state. It turns out [13], however, that for QKD purposes, detecting the error and using that information for postselection would provide us with an effective way to boost the key rate, and that error correction, as envisaged in the original protocol [7], may not be needed.

For the above process, a direct joint measurement on the nuclear spins of two separate, although possibly colocated, N- V centers may not be possible. To do a deterministic BSM on two separate nuclear spins here, we distribute an additional Bell pair between the corresponding electron spins of the two N- V centers. ES operations can then be performed by performing BSMs on the nuclear and electron spins within each N- V center [15]. This can be done by first applying a CNOT gate to the nuclear and electron spins, followed by relevant single-qubit measurements on each of the spins. Note that, in this procedure, we first have to measure the electron spin, and then map the nuclear spin state to the electron spin. The latter can be done by initializing the electron spin in an appropriate state and then performing a CNOT gate on the two spins with the nuclear spin as the control qubit. We can then measure the electron spin again, to effectively complete the measurement on the nuclear spin. A similar procedure can be used across the repeater chain. The measurement outcomes need to be notified to the end users to allow them adjust the Pauli frame on the final states, and/or for error-correction or postselection purposes.

Note that in the above procedure, the two N- V centers do not necessarily need to be colocated, and, in principle, one can assume an arbitrary distance between the two memories. That would, however, change the resilience of the system to memory decoherence. To study this, in the following, we define several protocols for different QR architectures, and analyze and compare them in the subsequent sections.

B. Quantum repeater structures and protocols

In this section, based on whether we employ coding or not, and how deterministic BSMs are done, we define four protocols, as explained below.

1. Protocols for encoded repeaters

Here, we describe the ideal implementation of the protocol proposed in Ref. [7] with three-qubit repetition codes on N- V -center platforms. We consider two architectures,

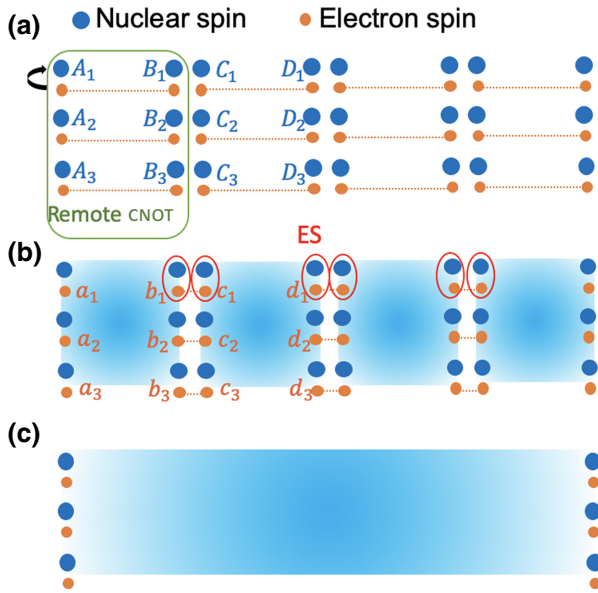


FIG. 2. Schematic QR structure for protocol 1, with the following steps: (a) Bell pairs are distributed between electron spins (small orange ovals) over all elementary links in a heralding way. The entangled states are transferred to and stored in the corresponding nuclear spins (large blue ovals), followed by a remote CNOT gate. (b) ES operations are performed on nuclear spins at intermediate nodes by creating temporary Bell pairs between the corresponding electron spins, and then performing a BSM within each N-V center. (c) The final encoded entangled state is created between the two end users. Based on the measurement results at each middle node, the Pauli frame of the final entangled state can be adjusted.

shown in Figs. 2 and 3, depending on whether the BSM is done on colocated N-V centers or on N-V centers separated by a distance L_0 , corresponding to the length of an elementary link. In both structures, there is a total of 2^n elementary links, where n is the nesting level of the corresponding QR.

In what we refer to as protocol 1 (P1), we use the structure in Fig. 2, and carry out the following steps:

(a) *Step 1.* Distribute encoded entanglement across all elementary links; see Sec. II A 2. As this requires multiple attempts to entangle all relevant pairs of N-V centers, we stop this process, whether or not all relevant pairs have been entangled, after a stoppage time T_1 and move on to the next step.

(b) *Step 2.* Perform BSMs at all intermediate nodes; see Sec. II A 3. We again stop this procedure, whether or not all relevant BSMs have been completed, after a stoppage time T_2 .

(c) *Step 3.* Pass all measurement results to the two end users. If there are missing entangled pairs or incomplete BSMs, then we discard the state generated in that round. We account for the effect of such discarded states in our key-rate analysis.

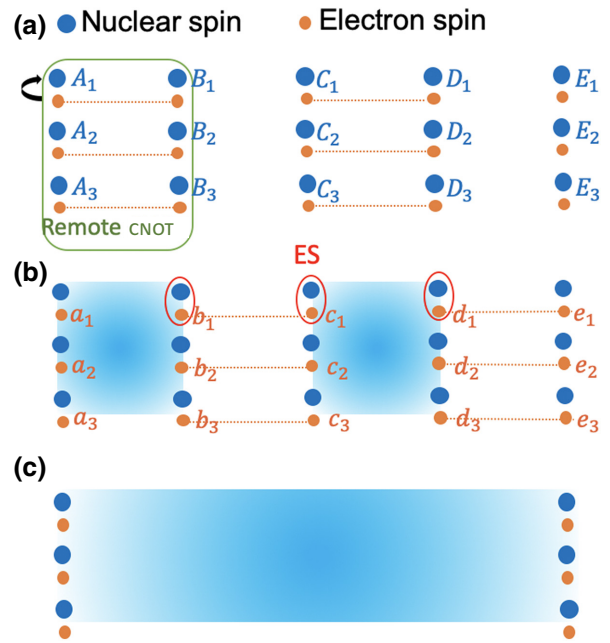


FIG. 3. Schematic QR structure for protocol 2, with the following steps: (a) Encoded Bell pairs are generated between nuclear spins in every other link. (b) Bell pairs are distributed between electron spins in all remaining links in order to facilitate a BSM within each N-V center at intermediate nodes. (c) The encoded entanglement is extended to the end users. Based on the measurement outcomes gathered from middle stations, one can adjust the Pauli frame of the final entangled state.

In what we call protocol 2 (P2), motivated by Refs. [16,17], we use the structure in Fig. 3, and carry out the following steps:

(a) *Step 1.* Distribute encoded entanglement across every other elementary link; see Sec. II A 2. We stop this process after a stoppage time T_1 and move on to the next step.

(b) *Step 2.* Distribute uncoded entanglement across the electron spins of all remaining links; see Sec. II A 1. We stop this process after a stoppage time T_2 and move on to the next step.

(c) *Step 3.* Perform BSMs at all intermediate nodes, which now contain only single N-V centers; see Sec. II A 3.

(d) *Step 4.* Pass all measurement results to the two end users. If there are missing entangled pairs or incomplete BSMs, then we discard the state generated in that round.

Protocol 2 requires fewer N-V centers and operations than does protocol 1, and, in that sense, may offer some advantage. But, in the end, what matters is the overall performance, normalized by the total number of memories used, which we use for comparison between such protocols.

2. Protocols for uncoded repeaters

In order to better understand whether QRs with encoding offer any advantages over their nonencoded versions, we also consider protocols 3 (P3) and 4 (P4) in this paper, which are the uncoded versions of protocols 1 and 2, respectively. For simplicity, we do not consider any distillations in protocols 3 and 4, as, without coding, that would turn them into probabilistic protocols. A comparison between encoded QRs and probabilistic ones is already available in Ref. [14]. In protocols 3 and 4, we just need to replace step 1 with the following revised step:

(a) *Step 1'*. Distribute Bell pairs between nuclear spins in all elementary links, for protocol 3, or every other elementary link, for protocol 4; see Sec. II A 1. We move on to the next step after a stoppage time T_1 .

The remaining steps are as in protocols 1 and 2, respectively.

C. Error models

In order to analyze the above QR setups, we consider three major sources of imperfections as follows:

(a) *Gate imperfections*. The CNOT gate for a control nuclear spin J and a target electron spin j within an N- V center is modeled as [1]

$$\rho^{\text{out}} = (1 - \beta)U_{Jj}\rho^{\text{in}}U_{Jj}^\dagger + \frac{\beta}{4}\text{Tr}_{Jj}(\rho^{\text{in}}) \otimes \mathbb{I}_{Jj}, \quad (3)$$

where ρ^{in} (ρ^{out}) is the input (output) before (after) the CNOT gate, and U_{Jj} represents the unitary operator corresponding to an ideal CNOT gate. The error in this two-qubit operation is modeled by a uniform depolarization of qubits J and j , represented by the identity operator \mathbb{I}_{Jj} , with probability β . We assume that a similar relationship to that in Eq. (3) would also model a CNOT gate with the electron (nuclear) spin as the control (target) qubit. While this is not necessarily the case, for simplicity, we assume that the parameter β is the same in both cases. With N- V centers, there are other common two-qubit gates, such as controlled-phase gates, that may be used in practice. Using equivalent quantum circuits, however, such operations can often be modeled by a CNOT gate, possibly with additional single-qubit rotations. In such cases, we assume that the parameter β captures the total error in the equivalent model. As in Refs. [13,14], we assume here that all single-qubit operations are perfect.

(b) *Measurement errors*. The projective measurements with respect to electron spin states $|0\rangle$ and $|1\rangle$ are represented by

$$\begin{aligned} P_0 &= (1 - \delta)|0\rangle\langle 0| + \delta|1\rangle\langle 1| \quad \text{and} \\ P_1 &= (1 - \delta)|1\rangle\langle 1| + \delta|0\rangle\langle 0|, \end{aligned} \quad (4)$$

respectively, where δ is the measurement error probability. Similar measurement operators, P_\pm , are used for projective measurements in the $|\pm\rangle = 1/\sqrt{2}(|0\rangle \pm |1\rangle)$ basis. The projective measurements of nuclear spins are modeled effectively in the same format but with error parameters $\beta/2 + \delta$, since there should always be a mapping operation performed through a CNOT gate as described in Sec. II A 3.

(c) *Decoherence*. We model the decoherence effect in electron and nuclear spins by using a depolarizing channel. For a single qubit a (A), after a waiting time t_w , the initial state ρ is mapped to

$$\begin{aligned} \mathcal{D}_{\text{depol}}^a(\rho) &= \lambda_2^e \rho + (1 - \lambda_2^e)(\mathbb{I}_2 - \rho), \\ \mathcal{D}_{\text{depol}}^A(\rho) &= \lambda_2^n \rho + (1 - \lambda_2^n)(\mathbb{I}_2 - \rho), \end{aligned} \quad (5)$$

where

$$\lambda_2^{e/n}(t_w) = \frac{1}{2} + \frac{e^{-t_w/\tau_{e/n}}}{2}, \quad (6)$$

with $\tau_{e/n}$ being the coherence time for electron or nuclear spins and \mathbb{I}_d being a $d \times d$ identity matrix. The expression in Eq. (5) is a rearranged form of the typical expression for a depolarizing channel, $p\rho + (1-p)\mathbb{I}_2/2$, with $p = \exp(-t_w/\tau_{e/n})$, in which $\lambda_2^{e/n}$ represents the fidelity of the output state with respect to the input state, in the case of pure input states. As shown below, this formulation suits better the two special cases of interest that we need to deal with in the setup under consideration. The first case of interest is when we have a two-qubit system in an initial entangled state such as $|\Phi^+\rangle_{AB(ab)}$ for the nuclear spins (electron spins). After a waiting time t_w , both spins decohere according to Eq. (5), resulting in $\mathcal{D}_{\text{depol}}^{AB}(|\Phi^+\rangle_{AB}\langle\Phi^+|)$ as the output state for the nuclear spins, where $\mathcal{D}_{\text{depol}}^{AB} = \mathcal{D}_{\text{depol}}^A \circ \mathcal{D}_{\text{depol}}^B$, and similarly for the electron spins. As shown in the Appendix, for $\rho = |\Phi^+\rangle_{AB(ab)}\langle\Phi^+|$, the output state can be written as

$$\begin{aligned} \mathcal{D}_{\text{depol}}^{AB}(\rho) &= \lambda_4^n \rho + (1 - \lambda_4^n)(\mathbb{I}_4 - \rho)/3, \\ \mathcal{D}_{\text{depol}}^{ab}(\rho) &= \lambda_4^e \rho + (1 - \lambda_4^e)(\mathbb{I}_4 - \rho)/3, \end{aligned} \quad (7)$$

where

$$\lambda_4^{e/n}(t_w) = \frac{1}{4}(3\lambda_2^{e/n}(t_w) - 1)^2 + \frac{3}{4}(1 - \lambda_2^{e/n}(t_w))^2 \quad (8)$$

is the fidelity of the output state with respect to the entangled input state. The same form as in Eq. (7) holds for any other Bell state, or any mixed state diagonal in Bell states, such as a Werner state. For a general two-qubit state, Eq. (7) acts as a conservative approximation to decoherence effects, given that it correctly specifies the fidelity of the output state while maximizing the noise by using a maximally mixed state for all other off-diagonal terms.

We use Eq. (7) to model decoherence across the elementary links as, in practical regions of interest, the deviations from a Bell-diagonal state are reasonably small. Note that the off-diagonal terms ignored in our approximation often do not contribute to the quantum bit-error rate (QBER) in QKD systems. The second case of interest is when the initial state is of the form $|\tilde{\Phi}^+\rangle_{\text{AB}}$, which is a six-qubit system, or a slight deviation from it. With similar calculations, we approximate the output state for an encoded entangled state ρ by

$$\mathcal{D}_{\text{depol}}^{\text{AB}}(\rho) = \lambda_{64}^n \rho + (1 - \lambda_{64}^n)(\mathbb{I}_{64} - \rho)/63, \quad (9)$$

where

$$\begin{aligned} \lambda_{64}^{e/n}(t_w) = & \frac{1}{64}[(3\lambda_2^{e/n}(t_w) - 1)^6 + 33(1 - \lambda_2^{e/n}(t_w))^6 \\ & + 15(3\lambda_2^{e/n}(t_w) - 1)^2(1 - \lambda_2^{e/n}(t_w))^4 \\ & + 15(3\lambda_2^{e/n}(t_w) - 1)^4(1 - \lambda_2^{e/n}(t_w))^2] \quad (10) \end{aligned}$$

is the fidelity of the output state with respect to the input state, if the initial state is the ideal encoded entangled state $|\tilde{\Phi}^+\rangle_{\text{AB}}$. Similarly to the two-qubit case, the above modeling of decoherence effectively treats all nondesired states as a maximally mixed state while correctly predicting the output fidelity; see the Appendix for more detail.

III. ERROR ANALYSIS

In order to assess how well N- V -center-based encoded QRs would operate, here we obtain the final distributed state as a function of the system parameters. In the case of measurement or gate errors, we have previously devised analytical and numerical techniques to accurately account for such issues and their impact on system performance [13,14]. In this paper, we additionally account for the effect of memory decoherence especially, because, in terms of coherence time, the electron spins in the N- V centers may impose some limitations on the achievable rate and distance.

Accounting in an analytical way for the decoherence effect in a system with many individual N- V centers, where each center decoheres on its own independently of the others, is not necessarily an easy task. In effect, we need to find the output state by averaging over all the random times by which the individual memories have decohered, considering the entangled nature of the links. Here, we devise an approximation technique in which, at each step along the way, we calculate the average waiting time for the memories involved, and then assume that all of them have decohered by the same average time. In this case, we need only to calculate the λ parameters in Eqs. (8) and (10) at the corresponding average waiting times of interest. This should provide us with a reasonable approximation to what

can be achieved in practice, which is what we are looking for here in the context of QKD as an application.

In the following, we calculate the relevant time parameters for each step of the proposed protocols and explain our methodology for obtaining the final state of the QR as a function of the system parameters.

A. Entanglement distribution

Here, we first obtain an entangled state distributed over an elementary link. This involves two steps: first, generating an entangled state between two electron spins, and then transferring that state to the corresponding nuclear spins. In both processes, we deviate from an ideal Bell pair because of gate errors and decoherence. We follow the two-photon protocol described in Sec. II A 1. For simplicity, we assume that the generated entangled state without any decoherence is the ideal Bell pair $|\Phi^+\rangle$. By the time that we hear about the success of the entanglement distribution, this ideal state of electron spins has already decohered during the time that it takes to transmit photons and learn about the success of the entanglement distribution protocol. In this paper, we assume that, compared with the transmission time (which for our setup is typically on the order of tens of microseconds or longer), the time that it takes for any local operation is negligible. In that case, this waiting time, or, effectively, the repetition period for the entanglement distribution protocol, is given by

$$T_0 = \frac{L_0}{c}, \quad (11)$$

where $L_0 = L_{\text{tot}}/2^n$ is the length of the elementary links, with L_{tot} being the total distance between the two end users and n being the nesting level. During this time, the desired target state $|\Phi^+\rangle$ decoheres in the electron spins, according to Eq. (7), yielding

$$\rho_{ee} = F_0|\Phi^+\rangle\langle\Phi^+| + \frac{1 - F_0}{3}(\mathbb{I}_4 - |\Phi^+\rangle\langle\Phi^+|), \quad (12)$$

which is a Werner state with

$$F_0 = \lambda_4^e(T_0), \quad (13)$$

where λ_4^e is given by Eq. (8).

This state is then immediately transferred to the corresponding nuclear spins. This is done by applying one CNOT gate at each end, with the electron spins as the control qubits and the nuclear spins in an initial state $|0\rangle$, followed by X measurements on the electron spins. This process is analytically simulated, according to Eqs. (3) and (4), by use of the symbolic software package *Mathematica* to give us the entangled state ρ_{nm} shared between two nuclear spins at a distance L_0 .

B. Encoded entanglement distribution

The next step in the encoded protocols is to create encoded entanglement across certain elementary links. In principle, once the three Bell pairs required in each leg have been established, we can proceed with a remote CNOT gate operation that distributes encoded entanglement across the corresponding link. In our proposed protocols, however, we wait for a time T_1 before we proceed to the ES stage. This means that the nuclear spins in our system have decohered for an average time of $\bar{T}_1 = T_1 - T_0/P_0(L_0)$, where

$$P_0(L_0) = \frac{1}{2}\eta_c^2\eta_i^2\eta_d^2 \quad (14)$$

is the success probability for each entanglement attempt. Here, η_c accounts for the emission probability of a ZPL photon from the N-V center, its collection and coupling efficiency into and out of the optical channel, and the efficiency of any required frequency conversion; η_d is the single-photon detector efficiency; and $\eta_i = \exp[-L_0/(2L_{\text{att}})]$ is the transmissivity for a photon through half of the elementary link. Note that, per elementary link, $1/P_0(L_0)$ is the average number of times that we have to repeat our entanglement distribution scheme until it succeeds. We have to repeat this process, in parallel, for M different pairs of memories, where, in protocol 1, $M = 3 \times 2^n$, in protocol 2, $M = 3 \times 2^{n-1}$, in protocol 3, $M = 2^n$, and in protocol 4, $M = 2^{n-1}$. Here, the waiting time for each memory pair is in itself a random variable, independent of, but identically distributed with, other waiting times; for all of these waiting times, the average waiting time is given by \bar{T}_1 . Even if we define a statistical average waiting-time variable $T_w = (1/M) \sum_{i=1}^M T_w^{(i)}$, where $T_w^{(i)}$ is the waiting time for the i th link, the expected value of T_w is equal to \bar{T}_1 , and its variance is expected to be small for large values of M , as is often the case for the structures of interest in the present work. In short, \bar{T}_1 properly captures the average decoherence time in this phase of our setup. As we will see later, \bar{T}_1 is indirectly a function of M , as our choice of T_1 depends on M .

Based on our average approach to accounting for decoherence across the repeater chain, we assume here that all nuclear spins have decohered for a time \bar{T}_1 by the time we apply the remote CNOT gate operation for an encoded repeater. This effect can be modeled by Eq. (7) using $\lambda_4^n(\bar{T}_1)$, with the input state $\rho = \rho_{nn}$. We then model the operations in the remote CNOT circuit shown in Fig. 1, accounting for operation and measurement errors [13,14], to obtain ρ'_{nn} as the output state for this stage of the protocol. Note that, for the remote CNOT operation, the electron spins are initialized into codeword states. This can be done, e.g., using techniques introduced in Refs. [45–47]. Based on these techniques, we assume in this paper that the codeword states are created error-free and that

the time that it takes to prepare them is embedded in T_1 . This is because the remote CNOT operation can be done at each elementary link once the three required Bell states for that link have been generated. That implies that, in terms of timing, the additional delay caused by the remote CNOT procedure, including the local preparation of the initial codeword states, matters only for the elementary link that is entangled last. Given that T_1 , in typical regimes of operation, is on the order of milliseconds, and local operations are assumed to be much faster, we neglect this additional timing parameter. If this is not the case in some experiment, the parameter T_1 can be adjusted accordingly for rate calculations. In protocols 3 and 4, we follow the same procedure but do not include the remote CNOT operation.

C. Entanglement swapping

Once encoded or uncoded entanglement has been stored in the nuclear spins, additional electron-electron entanglement is established so that ES operations can be performed at intermediate stations. For protocols 2 and 4, this process is the same as that for the distribution of the original Bell pairs, whereas in protocols 1 and 3, the Bell pairs are distributed over only a very short distance between two colocated electron spins. In the latter case, we assume that the corresponding electron-spin decoherence happens over a negligible time, whereas in the former case the electron-electron state has the same form as ρ_{ee} in Eq. (12).

Once electron-electron entanglement has been established, the corresponding ES operations between electron and nuclear spins are immediately performed. These ES operations can therefore be performed at different times for different memories. To estimate the decoherence during this step, and to follow the simple scheme that we adopt for decoherence analysis, we calculate the average time $\bar{T}_2(P_s) = T_s/P_s$ required to do ES operations across the repeater chain, where T_s denotes the repetition period of the electron-electron entangling attempts, and P_s denotes their success probability. During this time, our state ρ'_{nn} decoheres. For protocol 1, the decoherence is modeled by Eq. (9) with λ_{64}^n calculated at $t_w = \bar{T}_2[P_0(0)]$ and T_s being a small internal time constant. For protocol 2, the decoherence is modeled by Eq. (9) with λ_{64}^n calculated at $t_w = \bar{T}_2[P_0(L_0)]$ and $T_s = T_0$. For protocol 3, the decoherence is modeled by Eq. (7) with λ_4^n calculated at $t_w = \bar{T}_2[P_0(0)]$ and T_s being a small internal time constant. Finally, for protocol 4, the decoherence is modeled by Eq. (7) with λ_4^n calculated at $t_w = \bar{T}_2[P_0(L_0)]$ and $T_s = T_0$.

Let us denote the resulting state after the above decoherence process as ρ''_{nn} . Using the error models in Sec. II C and the techniques introduced in Refs. [13,14], we can then calculate the final output state of the QR, accounting for gate, measurement, and decoherence errors.

IV. QKD PERFORMANCE

It is interesting to compare different QR structures and protocols in terms of their performance for a concrete application. Here, we choose QKD as our benchmarking tool. We use the decoder modules proposed in Ref. [14], which rely only on single-qubit measurements, to generate a raw key bit. We also use the postselection technique proposed in Ref. [13], where only data points in which no errors have been detected in the ES stage are used for key generation. References [13,14] offer a detailed description of the analytical-numerical methods used to calculate the state shared between the two end users, from which secret-key rates are calculated in the present paper.

Here, we first calculate the secret-key generation rate per entangled state between Alice and Bob for the BBM92 protocol [48]. In the asymptotic limit, and for the efficient [49] entanglement-based QKD protocol, where one basis is used more often than the other, this parameter, known as the secret fraction [50], is given by

$$r_\infty = \text{Max}\{0, 1 - h(e_z) - h(e_x)\}, \quad (15)$$

where $h(p) = -p \log_2(p) - (1-p) \log_2(1-p)$ is the Shannon binary entropy function and e_i is the QBER in the measurement basis i , i.e., the probability that Alice and Bob get discordant measurement outcomes in that basis. Here, the secret fraction is calculated for the better of the two decoders proposed in Ref. [14], which already involves some postselection rules with regard to no errors in the ES stage, as well as those applied at the decoding stage. The authors of Ref. [14] explain how such postselection techniques can affect the key-rate parameters; for the sake of brevity, we do not repeat that here, but instead use the same techniques to find the key rate.

In order to obtain the total secret-key generation rate, we need to multiply the secret fraction by the entanglement generation rate R . Because of our assumption that the time for local operations and measurements is negligible, the overall timescale for the implementation of the protocols is determined by the sum of T_1 and T_2 . Thus, the rate for obtaining an entangled pair with a distance of L_{tot} is expressed as

$$R = \frac{P_S}{T_1 + T_2}, \quad (16)$$

where $P_S = P_{S1}P_{S2}$ denotes the probability that, in step 1, all required elementary links are successfully entangled *and*, in step 2, all relevant BSs are performed. The success probability for step 1 is given by $P_{S1} = (1 - (1 - q)^{T_1/T_0})^M$, and, in step 2, conditioned on success in step 1, by $P_{S2} = (1 - (1 - q)^{T_2/T_s})^M$, where, in each protocol, the corresponding values for q , M , and T_s are outlined in Table I. In this paper, we normalize the secret-key rate by

TABLE I. The relevant values of M , q , and T_s for calculating \bar{T}_1 , \bar{T}_2 , P_{S1} , and P_{S2} , for different protocols.

	\bar{T}_1, P_{S1}	\bar{T}_2, P_{S2}
Protocol 1	$M = 3 \times 2^n$, $q = P_0(L_0)$	$M = 3 \times (2^n - 1)$, $q = P_0(0), T_s$ fixed
Protocol 2	$M = 3 \times 2^{n-1}$, $q = P_0(L_0)$	$M = 3 \times 2^{n-1}$, $q = P_0(L_0), T_s = T_0$
Protocol 3	$M = 2^n$, $q = P_0(L_0)$	$M = 2^n - 1$, $q = P_0(0), T_s$ fixed
Protocol 4	$M = 3 \times 2^{n-1}$, $q = P_0(L_0)$	$M = 2^{n-1}$, $q = P_0(L_0), T_s = T_0$

the number of N-V centers to assess and compare the performance of the proposed protocols. The normalized key rate is given by

$$\begin{aligned} R_{\text{QKD}}^{\text{P1}} &= \frac{R^{\text{P1}} r_\infty^{\text{P1}}}{6 \times 2^n}, \\ R_{\text{QKD}}^{\text{P2}} &= \frac{R^{\text{P2}} r_\infty^{\text{P2}}}{3 \times (2^n + 1)}, \\ R_{\text{QKD}}^{\text{P3}} &= \frac{R^{\text{P3}} r_\infty^{\text{P3}}}{2^{n+1}}, \\ R_{\text{QKD}}^{\text{P4}} &= \frac{R^{\text{P4}} r_\infty^{\text{P4}}}{2^n + 1}, \end{aligned} \quad (17)$$

for protocols 1–4, respectively, as specified by the superscripts.

Based on the above expressions, we compare the secret-key generation rate, in the nominal mode of operation where no eavesdropper is present, for protocols 1–4. Our objective is to estimate the relevant parameters in Eq. (17) to get some insight into how these protocols are expected to perform in practice.

The nominal parameter values used in our numerical results are as follows. We fix both P_{S1} and P_{S2} at 0.99, from which T_1 and T_2 can be calculated for each protocol. Note that T_1 and T_2 are increasing functions of M , which indirectly affects the waiting or decoherence time in our protocols. For our set of parameters, T_1 and T_2 end up somewhere between 1.5 and 2 times the average time that it takes to entangle all relevant memory pairs. We then calculate \bar{T}_1 and \bar{T}_2 to estimate the effect of decoherence on our system. We set the coherence times of the electron and nuclear spins to $\tau_e = 10$ ms and $\tau_n = 1$ s, respectively, which are achievable in practice [41,51,52]. The above values reflect mostly the back action on the nuclear spins when the electron spins are being manipulated, but recent work with this type of memory [12,53–55] has shown some progress in resolving this issue. We therefore consider larger values of the coherence time in our numerical results as well. The detector efficiency is set to $\eta_d = 0.9$, which can be achieved by using superconducting single-photon detectors [56], offering negligible dark

counts in our case. The distribution time for next-to-each-other electron-electron entanglement is set to $T_s = 5 \mu\text{s}$, which is of the same order of magnitude as the timing of internal operations reported in Ref. [12]. We choose an optical fiber as our channel, with the speed of light in it being $c = 2 \times 10^5 \text{ km/s}$ and $L_{\text{att}} = 22 \text{ km}$.

Figure 4 illustrates the performance of different protocols for generating secret keys as a function of the CNOT gate error probability β , for an electron-spin measurement error probability of $\delta = 10^{-4}$ in the presence of depolarizing noise. We choose several different values for the coupling efficiency η_c , as well as three nominal distances of 100, 300, and 500 km. Such distances are perhaps too short to have an immediate impact in practice, but they are relevant to early demonstrations of quantum networks being pursued in, e.g., the Netherlands [12]. For each value of β , we find the optimum nesting level, denoted by n_{opt} on each curve, for each protocol, that maximizes the key rate in Eq. (17). Figures 4(a)–4(d) show the system performance for different combinations of the parameters. Note that in some parameter regimes, some protocols are not able to generate a positive key rate, and therefore are absent from the relevant graph. We can make several

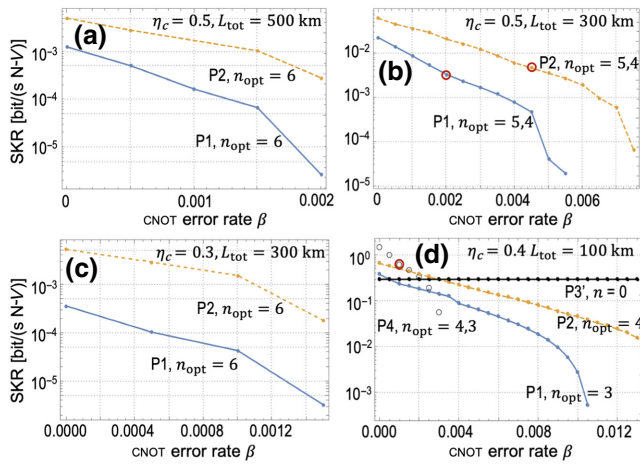


FIG. 4. Comparison of normalized secret-key rate (SKR) as a function of the CNOT error probability β for (a) $\eta_c = 0.5, L_{\text{tot}} = 500 \text{ km}$, (b) $\eta_c = 0.5, L_{\text{tot}} = 300 \text{ km}$, (c) $\eta_c = 0.3, L_{\text{tot}} = 300 \text{ km}$, and (d) $\eta_c = 0.4, L_{\text{tot}} = 100 \text{ km}$, for protocols 1–4. The result for a single entanglement distribution link between two electron spins, i.e., protocol 3' with $n = 0$, is also calculated [black solid curve in (d)]. The optimum nesting level, n_{opt} , is shown on each curve. Whenever the optimum nesting level changes as a function of β , the transition point is highlighted on the graph with a red circle. Up to this point, the optimum nesting level is the higher of the values given. From this point on, the lower value given becomes the optimum nesting level. The measurement error probability is set to $\delta = 10^{-4}$. The coherence times of the electron spins and nuclear spins are $\tau_e = 10 \text{ ms}$ and $\tau_n = 1 \text{ s}$, respectively.

interesting observations from this figure, as summarized below:

(a) *Observation 1.* Among the different values chosen in our simulation for the total distance, protocols 3 and 4 can generate nonzero secret-key rates for $L_{\text{tot}} = 100 \text{ km}$ only. For the chosen measurement-error-probability and coherence-time parameters, even if we improve the coupling efficiency to $\eta_c = 0.7$, there is still no key for $L_{\text{tot}} \geq 200 \text{ km}$ with these two protocols. This behavior occurs mainly because no distillation is considered in the uncoded repeaters. Given that conventional entanglement-distillation techniques that do not rely on quantum error-correction codes are probabilistic [5,6], it is not expected that they can offer any improvement in key-rate scaling either. The reason for this is that whenever we need to do a probabilistic operation, we need to repeat that until success is achieved. This requires additional classical communication to herald the success or failure of previous attempts, which results in additional delay and decoherence, both reducing the rate. This implies that for sufficiently short distances we may be better off not using any repeater nodes, and that one can instead distribute an entangled state directly between the far-end users. In this case, it suffices to distribute entanglement between two electron spins, and, once that has succeeded, to do the required QKD measurements directly on the electron spins. This case is shown by the horizontal black solid line in Fig. 4(d), and effectively represents the case for $n = 0$ with a modified version of protocol 3, where, in step 1', we do not do the additional operation of transferring electron spin states to the nuclear spins. We call this modified protocol P3', and its key rate is given by

$$R_0 = \frac{P_0(L_{\text{tot}}) \times r_{\infty}^{\text{P3}'}}{2T_0}. \quad (18)$$

Because of the low number of operations needed in such a scenario, P3' offers the best key rate for high values of β . Note that, in this case, we still suffer from some decoherence due to the transmission delay T_0 . For $L_{\text{tot}} = 100 \text{ km}$, if we restrict ourselves to $n \geq 1$, we observe that the highest secret-key rates are generated by protocol 4 for low values of β [open circles in Fig. 4(d)]. In this case, P4 always performs better than P3, so we do not show the latter on the graphs. The distance that can be covered by such uncoded QRs is, however, limited. This observation implies that, without any encoding, QR protocols may be able to cover only short distances, due to their low tolerance for errors.

(b) *Observation 2.* Among the four protocols, protocol 2 seems to offer the best performance across a wide range of parameters. It even outperforms protocol 1, which, at the cost of higher computational overhead, is expected to have the best error-correction and error-detection capabilities. One key reason for the superiority of protocol 2 in

our numerical examples seems to be the use of freshly created entangled states for its entanglement-distillation part, enabled here by error detection. To better understand this point, we need to compare the timing parameters for this protocol with those for protocol 1. The first point to note is that \bar{T}_1 is lower for P2 than for P1. This is because in protocol 1 there are more memory pairs that need to be entangled, and that makes T_1 , and consequently \bar{T}_1 , longer for this protocol than for protocol 2. For instance, for $L_{\text{tot}} = 300$ km, $\eta_c = 0.5$, and $n = 5$, \bar{T}_1 is roughly 0.0056 and 0.0051 s for P1 and P2, respectively. The second point is that in the entanglement-swapping stage, while \bar{T}_2 for protocol 2 is longer than that for protocol 1, it is typically much smaller than \bar{T}_1 . For instance, for the same parameters as above, \bar{T}_2 is roughly 49 and 709 μs for P1 and P2, respectively. This is because \bar{T}_2 corresponds to the entangling time for a single pair of memories, whereas \bar{T}_1 corresponds to the entangling time for many pairs. This results in $\bar{T}_1 + \bar{T}_2$, which is the average time for which the nuclear spins have decohered before the BSM is done, being comparable in the two protocols. In our example above, $\bar{T}_1 + \bar{T}_2$ is roughly 0.0056 and 0.0058 s for P1 and P2, respectively. Now, with this in mind, we can look at the situation when BSMs are performed in the two protocols. In P1, for error detection, we use pairs of entangled links that have both decohered for roughly $\bar{T}_1 + \bar{T}_2$. In P2, however, one entangled link has decohered for roughly $\bar{T}_1 + \bar{T}_2$, whereas the other link is freshly prepared and has decohered for only T_0 . Given that $\bar{T}_1 + \bar{T}_2$ is almost the same in the two protocols, this asymmetry in the quality of the entangled states used for distillation gives an edge to P2 over P1 and makes P2 more resistant, compared with P1, to decoherence issues.

We should also bear in mind that the figure of merit that we use is normalized to the number of N-V centers used, which, in the case of protocol 2, is almost half of that for protocol 1. This factor of 2, however, is compensated by the $T_1 + T_2$ term in Eq. (16), which, in the case of protocol 2, is less than 2 times that for protocol 1. In our example with $L_{\text{tot}} = 300$ km, $\eta_c = 0.5$, and $n = 5$, $T_1 + T_2$ is 0.0067 s for P1, versus 0.0116 s for P2. The overall effect is then governed mainly by the decoherence time discussed above, which is in favor of protocol 2.

(c) *Observation 3.* We notice that, for the optimum choice of nesting level, the internode distance varies roughly from 5 to 20 km. This, as we will see, is a function of other relevant parameters such as coherence times and coupling efficiencies, and can change slightly either way in certain regimes. But, generally speaking, this internode distance is more manageable than that for third-generation QRs, in which the nodes are only a few kilometers apart [57–62]. It is, however, more demanding than that for probabilistic QRs, where the internode distance can be on the order of tens of kilometers [4,63]. Another interesting observation is that, in some curves, the optimum nesting

level goes down with β . This can be attributed to the fact that for large values of β , it is better to have fewer nodes so that the total number of operations, and the error that is accumulated in the whole process, can be better managed.

To understand further how protocols 1 and 2 compare with each other, in Fig. 5, we investigate the sensitivity of these protocols to the total distance L_{tot} , the coupling efficiency η_c , and the coherence times of the nuclear and electron spins τ_n and τ_e . Figures 5(a) and 5(b) show the normalized key rate versus the total distance for two different sets of coherence times, where τ_n and τ_e in Fig. 5(b) are ten times those in Fig. 5(a). We observe that, in both figures, protocol 2 offers a higher key rate than does protocol 1 for the majority of distances. The two curves are closer for short distances, as the corresponding values of \bar{T}_1 are too short for the coherence times considered. The two curves are even closer initially in Fig. 5(b), where decoherence is less of an issue than in Fig. 5(a). Figure 5(b) also shows that such systems can cover distances in excess of 2000 km provided that the coherence times are sufficiently long. At 2000 km, the optimum value for L_0 is over 30 km. The optimum nesting level increases with the total distance, as expected.

The same tolerance to decoherence can be seen in Figs. 5(c) and 5(d), where we compare the two protocols versus η_c . Now the two curves get closer at high

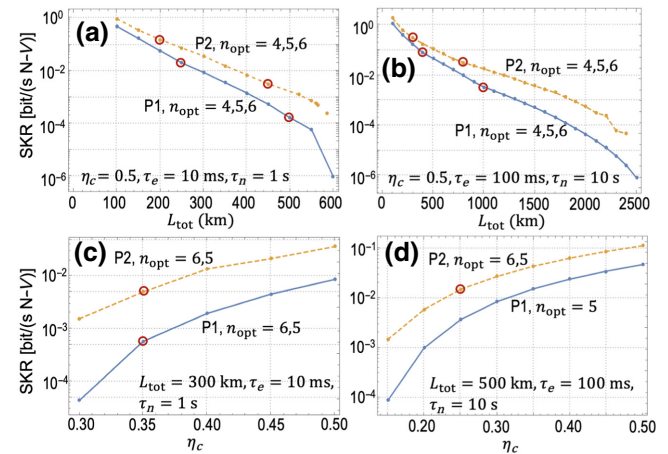


FIG. 5. Comparison of normalized secret-key rate as a function of the total distance L_{tot} for (a) $\eta_c = 0.5$, $\tau_e = 10$ ms, $\tau_n = 1$ s and (b) $\eta_c = 0.5$, $\tau_e = 100$ ms, $\tau_n = 10$ s, and as a function of η_c for (c) $L_{\text{tot}} = 300$ km, $\tau_e = 10$ ms, $\tau_n = 1$ s and (d) $L_{\text{tot}} = 500$ km, $\tau_e = 100$ ms, $\tau_n = 10$ s, for protocols 1 and 2. The CNOT gate error probability and the measurement error probability are $\beta = 10^{-3}$ and $\delta = 10^{-4}$, respectively. Again, we use red circles to indicate the points where the optimum nesting level, n_{opt} , changes. In (a),(b), the optimum nesting level for short distances is 4 and goes up by 1 at the red circles. In (c),(d), it starts at a higher number and decreases by 1 at the red circles.

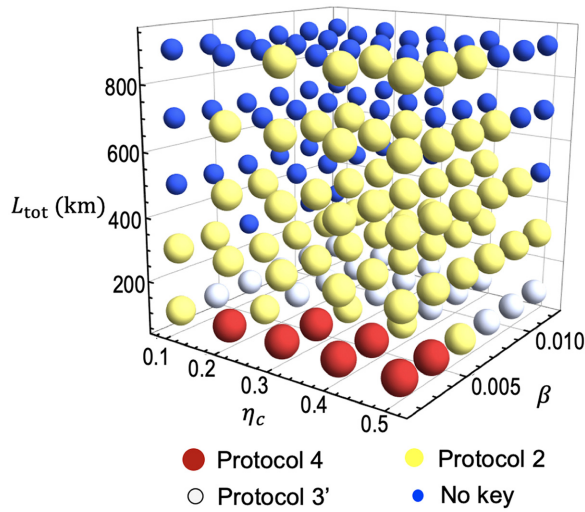


FIG. 6. Region plot showing the distribution of the optimal QR protocol in a three-dimensional parameter space for $\delta = 10^{-4}$, $\tau_e = 10$ ms, and $\tau_n = 10$ s.

values of η_c , which corresponds to shorter values of \bar{T}_1 and lower optimum nesting levels. For the range of parameter values considered in our numerical analysis, protocol 2 consistently offers higher key rates than does protocol 1.

Finally, in order to see which protocol performs best in different parameter regimes, in Fig. 6 we show a region plot highlighting the optimal QR structure that offers the highest key rate, for $\delta = 10^{-4}$, $\tau_e = 10$ ms, and $\tau_n = 10$ s, in a three-dimensional parameter space. We first note that, even with an improved nuclear coherence time, the uncoded QR protocols, i.e., protocols 3' and 4, offer the best performance at short distances only. For longer distances and larger error probabilities, protocol 2 is most often the optimal choice. This leads to the practical conclusion that, for near-term implementations, the partially encoded QRs, which use fewer resources, might be the best option.

V. CONCLUSION

In this paper, we analyze two quantum repeater protocols with three-qubit repetition codes on N-V centers on diamond platforms, with operation errors and decoherence noise being considered. We benchmark these encoded repeaters against uncoded structures by using QKD as a concrete application. We find that the uncoded QRs work at short distances only but possibly offer some advantage in such cases. For longer distances, QRs with encoding are the optimal choice. We notice that, in most practical regimes of interest, the protocol that relies on only partially encoded entangled states, hence consuming fewer physical resources, is the best-performing scheme. This leads to the conjecture that, for the future implementation

of encoded quantum repeaters, partially encoded structures, rather than a fully encoded structure, are of more practical use.

It is worth highlighting that, in any practical setup, there might be other parameters and processes that need to be properly modeled and accounted for in order to get a closer match to the experimental results. The work presented here offers some insight into and preliminary predictions of what we may expect with such experimental setups, but it does not replace the need for more accurate calculations when it comes to implementing such setups. Nevertheless, the results that we obtain here are promising in at least two respects. First, they indicate that the required parameter regime for a reasonably good operational quantum repeater setup is not far out of reach. Second, while the focus in experimental efforts today is mostly on the simplest repeater structures, our work here shows that certain encoded structures should not be ruled out at this stage and can be part of our experimental agenda in the coming years.

ACKNOWLEDGMENTS

This project is funded by the European Union's Horizon 2020 Research and Innovation Programme under the Marie Skłodowska-Curie Grant No. 675662 (QCALL) and the UK EPSRC Grant No. EP/M013472/1. The data generated in this work can be reproduced by means of the methodology and equations given in this paper.

APPENDIX: DERIVATION OF DECOHERENCE PARAMETERS

The decoherence model in Eq. (5) for a single-qubit system, where $d = 2$, can be rewritten as

$$\begin{aligned}
 \mathcal{D}_{\text{depol}}(\rho) &= \lambda_2 \rho + (1 - \lambda_2)(\mathbb{I}_2 - \rho) \\
 &= (2\lambda_2 - 1)\rho + (1 - \lambda_2)\mathbb{I}_2 \\
 &= (2\lambda_2 - 1)\rho + (1 - \lambda_2) \\
 &\quad \times \frac{\rho + X\rho X + Y\rho Y + Z\rho Z}{2} \\
 &= \frac{3\lambda_2 - 1}{2}\rho + \frac{1 - \lambda_2}{2}(X\rho X + Y\rho Y + Z\rho Z),
 \end{aligned} \tag{A1}$$

where X , Y , and Z are Pauli operations. For a two-qubit system, each qubit decoheres independently, which leads to

$$\begin{aligned} \mathcal{D}_{\text{depol}}^A \circ \mathcal{D}_{\text{depol}}^B(\rho_{AB}) = & \left(\frac{3\lambda_2 - 1}{2}\right)^2 \rho_{AB} + \frac{(3\lambda_2 - 1)(1 - \lambda_2)}{4} \left[(X_B, Y_B, Z_B)\rho_{AB} \begin{pmatrix} X_B \\ Y_B \\ Z_B \end{pmatrix} + (X_A, Y_A, Z_A)\rho_{AB} \begin{pmatrix} X_A \\ Y_A \\ Z_A \end{pmatrix} \right] \\ & + \left(\frac{1 - \lambda_2}{2}\right)^2 (X_A, Y_A, Z_A)(X_B, Y_B, Z_B)\rho_{AB} \begin{pmatrix} X_A \\ Y_A \\ Z_A \end{pmatrix} \begin{pmatrix} X_B \\ Y_B \\ Z_B \end{pmatrix}. \end{aligned} \quad (\text{A2})$$

If the state ρ_{AB} is a Bell-diagonal state, we can verify that the output state obtained from Eq. (A2) is equivalent to Eq. (7). Note that, in Eq. (A2), a Bell state remains intact when operated on by the following operators: $\mathbb{I}_A \mathbb{I}_B$, $X_A X_B$, $Y_A Y_B$, and $Z_A Z_B$. Therefore, the fidelity of the output state with respect to the input Bell state is given by the sum of the corresponding coefficients in Eq. (A2):

$$\lambda_4 = \frac{1}{4}(3\lambda_2 - 1)^2 + \frac{3}{4}(1 - \lambda_2)^2, \quad (\text{A3})$$

which is the same as Eq. (8).

To obtain the decoherence effect in a six-qubit system, we have to apply the single-qubit depolarizing model of Eq. (5) to each qubit independently, and calculate the tandem effect. This results in a lengthy expression for the output state, which we will not reproduce here. But, it can be verified that the operators that map the encoded Bell state $|\tilde{\Phi}^+\rangle_{\text{AB}}$ to itself are given by $\mathbb{I}^{\otimes 6}$, $X^{\otimes 6}$, $Y^{\otimes 6}$, $Z^{\otimes 6}$, $X^{\otimes 2} Y^{\otimes 4}$, $X^{\otimes 4} Y^{\otimes 2}$, $Z^{\otimes 4} \mathbb{I}^{\otimes 2}$, and $Z^{\otimes 2} \mathbb{I}^{\otimes 4}$. Again, one can calculate the corresponding fidelity for the output state, with respect to $|\tilde{\Phi}^+\rangle_{\text{AB}}$, by accounting for the coefficients of the relevant terms to obtain

$$\begin{aligned} \lambda_{64} = & \frac{1}{64}[(3\lambda_2 - 1)^6 + 33(1 - \lambda_2)^6 \\ & + 15(3\lambda_2 - 1)^2(1 - \lambda_2)^4 \\ & + 15(3\lambda_2 - 1)^4(1 - \lambda_2)^2], \end{aligned} \quad (\text{A4})$$

which is equivalent to Eq. (10).

-
- [1] H.-J. Briegel, W. Dür, J. I. Cirac, and P. Zoller, Quantum Repeaters: The Role of Imperfect Local Operations in Quantum Communication, *Phys. Rev. Lett.* **81**, 5932 (1998).
 - [2] W. Dür, H.-J. Briegel, J. Cirac, and P. Zoller, Quantum Repeaters Based on Entanglement Purification, *Phys. Rev. A* **59**, 169 (1999).
 - [3] L.-M. Duan, M. Lukin, J. I. Cirac, and P. Zoller, Long-distance quantum communication with atomic ensembles and linear optics, *Nature* **414**, 413 (2001).
 - [4] N. Sangouard, C. Simon, H. De Riedmatten, and N. Gisin, Quantum repeaters based on atomic ensembles and linear optics, *Rev. Mod. Phys.* **83**, 33 (2011).

- [5] C. H. Bennett, G. Brassard, S. Popescu, B. Schumacher, J. A. Smolin, and W. K. Wootters, Purification of Noisy Entanglement and Faithful Teleportation via Noisy Channels, *Phys. Rev. Lett.* **76**, 722 (1996).
- [6] D. Deutsch, A. Ekert, R. Jozsa, C. Macchiavello, S. Popescu, and A. Sanpera, Quantum Privacy Amplification and the Security of Quantum Cryptography over Noisy Channels, *Phys. Rev. Lett.* **77**, 2818 (1996).
- [7] L. Jiang, J. M. Taylor, K. Nemoto, W. J. Munro, R. Van Meter, and M. D. Lukin, Quantum Repeater with Encoding, *Phys. Rev. A* **79**, 032325 (2009).
- [8] F. Jelezko, T. Gaebel, I. Popa, M. Domhan, A. Gruber, and J. Wrachtrup, Observation of Coherent Oscillation of a Single Nuclear Spin and Realization of a Two-Qubit Conditional Quantum Gate, *Phys. Rev. Lett.* **93**, 130501 (2004).
- [9] G. Waldherr, Y. Wang, S. Zaiser, M. Jamali, T. Schulte-Herbrüggen, H. Abe, T. Ohshima, J. Isoya, J. Du, and P. Neumann, *et al.*, Quantum error correction in a solid-state hybrid spin register, *Nature* **506**, 204 (2014).
- [10] T. H. Taminiu, J. Cramer, T. van der Sar, V. V. Dobrovitski, and R. Hanson, Universal control and error correction in multi-qubit spin registers in diamond, *Nat. Nanotechnol.* **9**, 171 (2014).
- [11] S. B. van Dam, P. C. Humphreys, F. Rozpędek, S. Wehner, and R. Hanson, Multiplexed entanglement generation over quantum networks using multi-qubit nodes, *Quantum Sci. Technol.* **2**, 034002 (2017).
- [12] M. Pompili, S. L. Hermans, S. Baier, H. K. Beukers, P. C. Humphreys, R. N. Schouten, R. F. Vermeulen, M. J. Tiggeleman, L. dos Santos Martins, and B. Dirkse, *et al.*, Realization of a multinode quantum network of remote solid-state qubits, *Science* **372**, 259 (2021).
- [13] Y. Jing, D. Alsina, and M. Razavi, Quantum Key Distribution over Quantum Repeaters with Encoding: Using Error Detection as an Effective Postselection Tool, *Phys. Rev. Appl.* **14**, 064037 (2020).
- [14] Y. Jing and M. Razavi, Simple Efficient Decoders for Quantum Key Distribution over Quantum Repeaters with Encoding, *Phys. Rev. Appl.* **15**, 044027 (2021).
- [15] S. E. Vinay and P. Kok, Practical Repeaters for Ultralong-Distance Quantum Communication, *Phys. Rev. A* **95**, 052336 (2017).
- [16] L. Childress, J. Taylor, A. S. Sørensen, and M. Lukin, Fault-Tolerant Quantum Communication Based on Solid-State Photon Emitters, *Phys. Rev. Lett.* **96**, 070504 (2006).
- [17] L. Childress, J. Taylor, A. S. Sørensen, and M. D. Lukin, Fault-Tolerant Quantum Repeaters with Minimal Physical Resources and Implementations Based on Single-Photon Emitters, *Phys. Rev. A* **72**, 052330 (2005).

- [18] H.-R. Wei and F.-G. Deng, Compact Quantum Gates on Electron-Spin Qubits Assisted by Diamond Nitrogen-Vacancy Centers inside Cavities, *Phys. Rev. A* **88**, 042323 (2013).
- [19] M. S. Everitt, S. Devitt, W. Munro, and K. Nemoto, High-Fidelity Gate Operations with the Coupled Nuclear and Electron Spins of a Nitrogen-Vacancy Center in Diamond, *Phys. Rev. A* **89**, 052317 (2014).
- [20] D. D. Awschalom, R. Hanson, J. Wrachtrup, and B. B. Zhou, Quantum technologies with optically interfaced solid-state spins, *Nat. Photonics* **12**, 516 (2018).
- [21] M. W. Doherty, N. B. Manson, P. Delaney, F. Jelezko, J. Wrachtrup, and L. C. Hollenberg, The nitrogen-vacancy colour centre in diamond, *Phys. Rep.* **528**, 1 (2013).
- [22] M. G. Dutt, L. Childress, L. Jiang, E. Togan, J. Maze, F. Jelezko, A. Zibrov, P. Hemmer, and M. Lukin, Quantum register based on individual electronic and nuclear spin qubits in diamond, *Science* **316**, 1312 (2007).
- [23] P. Neumann, J. Beck, M. Steiner, F. Rempp, H. Fedder, P. R. Hemmer, J. Wrachtrup, and F. Jelezko, Single-shot readout of a single nuclear spin, *Science* **329**, 542 (2010).
- [24] P. E. Barclay, K.-M. C. Fu, C. Santori, A. Faraon, and R. G. Beausoleil, Hybrid Nanocavity Resonant Enhancement of Color Center Emission in Diamond, *Phys. Rev. X* **1**, 011007 (2011).
- [25] R. Epstein, F. Mendoza, Y. Kato, and D. Awschalom, Anisotropic interactions of a single spin and dark-spin spectroscopy in diamond, *Nat. Phys.* **1**, 94 (2005).
- [26] B. J. M. Hausmann, B. J. Shields, Q. Quan, Y. Chu, N. P. de Leon, R. Evans, M. J. Burek, A. S. Zibrov, M. Markham, and D. Twitchen, *et al.*, Coupling of NV centers to photonic crystal nanobeams in diamond, *Nano Lett.* **13**, 5791 (2013).
- [27] M. Ruf, M. J. Weaver, S. B. van Dam, and R. Hanson, Resonant Excitation and Purcell Enhancement of Coherent Nitrogen-Vacancy Centers Coupled to a Fabry-Perot Microcavity, *Phys. Rev. Appl.* **15**, 024049 (2021).
- [28] S. Bogdanović, S. B. van Dam, C. Bonato, L. C. Coenen, A.-M. J. Zwerver, B. Hensen, M. S. Liddy, T. Fink, A. Reiserer, and M. Lončar, *et al.*, Design and low-temperature characterization of a tunable microcavity for diamond-based quantum networks, *Appl. Phys. Lett.* **110**, 171103 (2017).
- [29] K. Nemoto, M. Trupke, S. J. Devitt, A. M. Stephens, B. Scharfenberger, K. Buczak, T. Nöbauer, M. S. Everitt, J. Schmiedmayer, and W. J. Munro, Photonic Architecture for Scalable Quantum Information Processing in Diamond, *Phys. Rev. X* **4**, 031022 (2014).
- [30] D. Riedel, I. Söllner, B. J. Shields, S. Starosielec, P. Appel, E. Neu, P. Maletinsky, and R. J. Warburton, Deterministic Enhancement of Coherent Photon Generation from a Nitrogen-Vacancy Center in Ultrapure Diamond, *Phys. Rev. X* **7**, 031040 (2017).
- [31] D. Le Sage, L. M. Pham, N. Bar-Gill, C. Belthangady, M. D. Lukin, A. Yacoby, and R. L. Walsworth, Efficient Photon Detection from Color Centers in a Diamond Optical Waveguide, *Phys. Rev. B* **85**, 121202 (2012).
- [32] A. Faraon, P. E. Barclay, C. Santori, K.-M. C. Fu, and R. G. Beausoleil, Resonant enhancement of the zero-phonon emission from a colour centre in a diamond cavity, *Nat. Photonics* **5**, 301 (2011).
- [33] M. K. Bhaskar, R. Riedinger, B. Machielse, D. S. Levonian, C. T. Nguyen, E. N. Knall, H. Park, D. Englund, M. Lončar, D. D. Sukachev, and M. D. Lukin, Experimental demonstration of memory-enhanced quantum communication, *Nature* **580**, 60 (2020).
- [34] H. Bernien, L. Childress, L. Robledo, M. Markham, D. Twitchen, and R. Hanson, Two-Photon Quantum Interference from Separate Nitrogen Vacancy Centers in Diamond, *Phys. Rev. Lett.* **108**, 043604 (2012).
- [35] W. Pfaff, B. J. Hensen, H. Bernien, S. B. van Dam, M. S. Blok, T. H. Taminiau, M. J. Tiggelman, R. N. Schouten, M. Markham, and D. J. Twitchen, *et al.*, Unconditional quantum teleportation between distant solid-state quantum bits, *Science* **345**, 532 (2014).
- [36] B. Hensen, H. Bernien, A. E. Dréau, A. Reiserer, N. Kalb, M. S. Blok, J. Ruitenberg, R. F. Vermeulen, R. N. Schouten, and C. Abellán, *et al.*, Loophole-free Bell inequality violation using electron spins separated by 1.3 km, *Nature* **526**, 682 (2015).
- [37] C. Cabrillo, J. I. Cirac, P. Garcia-Fernandez, and P. Zoller, Creation of Entangled States of Distant Atoms by Interference, *Phys. Rev. A* **59**, 1025 (1999).
- [38] P. C. Humphreys, N. Kalb, J. P. Morits, R. N. Schouten, R. F. Vermeulen, D. J. Twitchen, M. Markham, and R. Hanson, Deterministic delivery of remote entanglement on a quantum network, *Nature* **558**, 268 (2018).
- [39] F. Rozpędek, R. Yehia, K. Goodenough, M. Ruf, P. C. Humphreys, R. Hanson, S. Wehner, and D. Elkouss, Near-Term Quantum-Repeater Experiments with Nitrogen-Vacancy Centers: Overcoming the Limitations of Direct Transmission, *Phys. Rev. A* **99**, 052330 (2019).
- [40] S. D. Barrett and P. Kok, Efficient High-Fidelity Quantum Computation Using Matter Qubits and Linear Optics, *Phys. Rev. A* **71**, 060310 (2005).
- [41] H. Bernien, B. Hensen, W. Pfaff, G. Koolstra, M. S. Blok, L. Robledo, T. Taminiau, M. Markham, D. J. Twitchen, and L. Childress, *et al.*, Heralded entanglement between solid-state qubits separated by three metres, *Nature* **497**, 86 (2013).
- [42] N. Lo Piparo, M. Razavi, and W. J. Munro, Measurement-Device-Independent Quantum Key Distribution with Nitrogen Vacancy Centers in Diamond, *Phys. Rev. A* **95**, 022338 (2017).
- [43] N. Lo Piparo, M. Razavi, and W. J. Munro, Memory-Assisted Quantum Key Distribution with a Single Nitrogen-Vacancy Center, *Phys. Rev. A* **96**, 052313 (2017).
- [44] P. Neumann, N. Mizuochi, F. Rempp, P. Hemmer, H. Watanabe, S. Yamasaki, V. Jacques, T. Gaebel, F. Jelezko, and J. Wrachtrup, Multipartite entanglement among single spins in diamond, *Science* **320**, 1326 (2008).
- [45] N. K. Bernardes and P. van Loock, Hybrid Quantum Repeater with Encoding, *Phys. Rev. A* **86**, 052301 (2012).
- [46] A. Zheng, J. Li, R. Yu, X.-Y. Lü, and Y. Wu, Generation of Greenberger-Horne-Zeilinger state of distant diamond nitrogen-vacancy centers via nanocavity input-output process, *Opt. Express* **20**, 16902 (2012).
- [47] L.-Y. Cheng, H.-F. Wang, S. Zhang, and K.-H. Yeon, Quantum state engineering with nitrogen-vacancy centers coupled to low- Q microresonator, *Opt. Express* **21**, 5988 (2013).

- [48] C. H. Bennett, G. Brassard, and N. D. Mermin, Quantum Cryptography without Bell's Theorem, *Phys. Rev. Lett.* **68**, 557 (1992).
- [49] H.-K. Lo, H. F. Chau, and M. Ardehali, Efficient quantum key distribution scheme and a proof of its unconditional security, *J. Cryptol.* **18**, 133 (2005).
- [50] V. Scarani, H. Bechmann-Pasquinucci, N. J. Cerf, M. Dušek, N. Lütkenhaus, and M. Peev, The security of practical quantum key distribution, *Rev. Mod. Phys.* **81**, 1301 (2009).
- [51] N. Bar-Gill, L. M. Pham, A. Jarmola, D. Budker, and R. L. Walsworth, Solid-state electronic spin coherence time approaching one second, *Nat. Commun.* **4**, 1 (2013).
- [52] P. C. Maurer, G. Kucsko, C. Latta, L. Jiang, N. Y. Yao, S. D. Bennett, F. Pastawski, D. Hunger, N. Chisholm, and M. Markham, *et al.*, Room-temperature quantum bit memory exceeding one second, *Science* **336**, 1283 (2012).
- [53] M. H. Abobeih, J. Cramer, M. A. Bakker, N. Kalb, M. Markham, D. J. Twitchen, and T. H. Taminiau, One-second coherence for a single electron spin coupled to a multi-qubit nuclear-spin environment, *Nat. Commun.* **9**, 1 (2018).
- [54] N. Kalb, P. C. Humphreys, J. Slim, and R. Hanson, Dephasing Mechanisms of Diamond-Based Nuclear-Spin Memories for Quantum Networks, *Phys. Rev. A* **97**, 062330 (2018).
- [55] C. Bradley, J. Randall, M. H. Abobeih, R. Berrevoets, M. Degen, M. Bakker, M. Markham, D. Twitchen, and T. H. Taminiau, A Ten-Qubit Solid-State Spin Register with Quantum Memory up to One Minute, *Phys. Rev. X* **9**, 031045 (2019).
- [56] J. Zhang, M. A. Itzler, H. Zbinden, and J.-W. Pan, Advances in InGaAs/InP single-photon detector systems for quantum communication, *Light: Sci. Appl.* **4**, e286 (2015).
- [57] S. Muralidharan, J. Kim, N. Lütkenhaus, M. D. Lukin, and L. Jiang, Ultrafast and Fault-Tolerant Quantum Communication across Long Distances, *Phys. Rev. Lett.* **112**, 250501 (2014).
- [58] J. Borregaard, H. Pichler, T. Schröder, M. D. Lukin, P. Lodahl, and A. S. Sørensen, One-Way Quantum Repeater Based on Near-Deterministic Photon-Emitter Interfaces, *Phys. Rev. X* **10**, 021071 (2020).
- [59] K. Azuma, K. Tamaki, and H.-K. Lo, All-photonic quantum repeaters, *Nat. Commun.* **6**, 1 (2015).
- [60] A. N. Glaudell, E. Waks, and J. M. Taylor, Serialized quantum error correction protocol for high-bandwidth quantum repeaters, *New J. Phys.* **18**, 093008 (2016).
- [61] F. Ewert and P. van Loock, Ultrafast Fault-Tolerant Long-Distance Quantum Communication with Static Linear Optics, *Phys. Rev. A* **95**, 012327 (2017).
- [62] S.-W. Lee, T. C. Ralph, and H. Jeong, Fundamental Building Block for All-Optical Scalable Quantum Networks, *Phys. Rev. A* **100**, 052303 (2019).
- [63] N. L. Piparo and M. Razavi, Long-Distance Quantum Key Distribution with Imperfect Devices, *Phys. Rev. A* **88**, 012332 (2013).